Available online at www.sciencedirect.com

jmr&t Journal of Materials Research and Technology

https://www.journals.elsevier.com/journal-of-materials-research-and-technology

Original Article

New synthesis route to kesterite Cu_2ZnSnS_4 semiconductor nanocrystalline powders utilizing copper alloys and a high energy ball milling-assisted process

Katarzyna Kapusta[a], *Mariusz Drygas*[a,*], *Jerzy F. Janik*[a], *Zbigniew Olejniczak*[b]

[a] *AGH University of Science and Technology, Faculty of Energy and Fuels, Al. Mickiewicza 30, 30-059 Krakow, Poland*
[b] *Institute of Nuclear Physics, Polish Academy of Sciences, ul. Radzikowskiego 152, 31-342 Krakow, Poland*

ARTICLE INFO

Article history:
Received 16 June 2020
Accepted 11 September 2020
Available online 30 September 2020

Keywords:
Kesterite
Copper alloy
Nanocrystalline powders
Mechanochemical synthesis
Photovoltaics

ABSTRACT

Presented is a new mechanochemically assisted synthesis route to kesterite Cu_2ZnSnS_4 semiconductor for perspective photovoltaic applications. Initially, the combined copper Cu, zinc Zn, and tin Sn powders in atomic ratio 2:1:1 were subjected to high energy ball milling in a planetary ball mill under the highest reported to date rotation speeds of 900 and 1000 rpm to yield a definite nanopowder mixture of the copper intermetallic phases, *i.e.*, γ Cu_5Zn_8-type and η' Cu_6Sn_5-type of non-stoichiometric compositions. Upon addition of a suitable amount of sulfur S, the reactive milling was continued affording a pure sphalerite-type cubic phase tentatively called a pre-kesterite. As expected from our earlier research, this by-product did not exhibit any ^{65}Cu and ^{119}Sn MAS NMR spectra or clearly-defined absorption in the UV–vis range. The disordered and very much random Cu-Zn-Sn metal site occupation of all metal layers in the structure is proposed to account for the observed properties of pre-kesterite. The subsequent annealing under argon at temperatures around 500–550 °C resulted in the cubic phase conversion to the tetragonal phase of kesterite, prevailingly, by metal center reconfiguration into distinct Cu-Sn and Cu-Zn layers accompanied by crystal growth/particle recrystallization. The micro-Raman spectra were consistent with similar bonding and lattice phonon characteristics in both related materials. The XPS data confirmed the same oxidation states and comparable energy level characteristics of the constituent elements. The annealed nanocrystalline powders showed the anticipated ^{65}Cu and ^{119}Sn MAS NMR features, while supporting remnant paramagnetism, and UV–vis semiconducting characteristics of the target kesterite.

* *Corresponding author.*
E-mail: madrygas@agh.edu.pl (M. Drygas).
https://doi.org/10.1016/j.jmrt.2020.09.062

1. Introduction

In search for efficient, low cost, and environment-friendly materials that might contest silicon Si in modern photovoltaic applications, significant research effort has been focused on the quaternary compound semiconductor Cu_2ZnSnS_4 that, based on mineralogy nomenclature, is customarily called kesterite and often is cited in short as CZTS [1–3]. It appears that some related copper compounds derived by substituting zinc Zn by other metals (*e.g.*, iron Fe) or sulfur S by a suitable chalcogen (*e.g.*, selenium Se) may have even more advantageous semiconducting and optical properties for this kind of applications. The best pure kesterite-based thin film photovoltaic cell efficiencies have presently reached values nearing 10% [4] whereas for some substituted kesterites a few percent higher values have been reported [5] with the theoretical conversion efficiency limit of 32.2% [6]. In this regard, kesterite nanocrystalline powders are considered for the inorganic part of nano-contacts of the specific inorganic-organic photovoltaic cells or as a substrate for preparing CZTS inks to be eventually used in making thin film cells.

In addition to striving to achieve higher and higher cell efficiencies, there is still a need to develop a reproducible and cost-effective kesterite preparation method including kesterite powders. The mechanochemical synthesis method that relies on high energy ball milling of solid reagents, preferably, in a planetary ball mill offers here both the relative simplicity, high degree of automation, and significant efficiency and yield advantages [7–9]. The major processing parameters include relative weights of the balls and precursor in a milling bowl, ball diameter, rotation speed, milling time, and dry or "wet" milling conditions. An eventual application of a dispersion liquid (wet conditions) is intended to minimize milling ball abrasion and adventitious product contamination. At present, milling bowls with volumes of several tens of mL and rotation speeds of 1000 rpm and higher are available in laboratory practice. Due to diffusion limited solid state reactions of the milled mixtures, reaction times of the order of several and more hours are quite typical.

Since the target Cu_2ZnSnS_4 is a multinary metal sulfide, a conceptually obvious approach is to react a stoichiometric mixture of the respective metal sulfides, *i.e.*, CuS (or Cu_2S), ZnS, and SnS (or SnS_2). In the extensive studies of the system, high energy dry ball milling of the sulfides at 350–400 rpm for up to 3–5 h afforded a raw product of low crystallinity with a supposed tetragonal "kesterite-type structure" (I-4), which required further heating up to 500 °C to yield well crystallized bulk kesterite nanopowders [10–12]. In the somewhat related investigations, Cu_2S, ZnS, SnS_2, and S powders were wet (ethanol) ball milled at 350 rpm, 8 h, and the resulting product was pressed into a pellet that was sintered under argon at 700 °C, 4 h; the sintered body was used to make kesterite films on glass supports by RF sputtering at 350–500 °C [13]. Similarly, suitable powder mixtures of CuS, ZnS, and SnS_2 were ball milled at 300 rpm, 3 h, and sintered under pressure into pellets at 200–600 °C, 8 h, with the latter under selected conditions shown to consist of tetragonal kesterite; the pellets were further used as a material source in RF sputtering experiments to make films of kesterite on the Mo/glass [14].

There are several reports available on reacting mixtures of the relatively inexpensive constituent elements, *i.e.*, Cu, Zn, Sn, S under mechanochemical conditions directed in many cases towards thin film preparation for solar cells. The first study on such a system from 2011 applied planetary ball milling with rotation speeds up to 600 rpm [15]. The one-step synthesis was completed after 20 h and resulted in nanocrystalline powders of what was claimed to be kesterite of an av. 9–10 nm particle size and arguably resolved as a tetragonal phase belonging to the I-42 m space group. Much shorter times of the order of 20 min at 800 rpm were used to prepare raw powders from the milled elements including Se [16]. Such by-products were annealed at 550 °C, 3 h, to result in a "tetragonal kesterite-type" powders (I-4), which were then used in a form of ink to make prototype kesterite thin layers. In the related studies of the mechanochemical route to such films, dry milling of the elements at 500 rpm, up to 5 h [17] or at 750 rpm, up to 60 h [18] was arguably claimed to afford tetragonal kesterite (I-42 m) without any additional annealing. In an alternative approach, raw nanopowders were prepared *via* wet (1-butanol) milling of the elements (S or Se) at 450 rpm, 30 h, which were in the next step applied as thin films on a glass support to be eventually annealed at 500 °C, 5 min [19]. For CZST, both the raw powders, av. particle size *ca.* 8–10 nm, and the annealed products, av. particle size *ca.* 26–44 nm, were indexed as belonging to the tetragonal space group I-42 m. In yet another attempt, wet (deionized water) ball milling of the constituent elements at 400–580 rpm, up to 48 h, already after 3 h appeared to produce the tetragonal phase of kesterite nanopowders [20]. They were used to make pressed pellets that were sintered at 550–700 °C, 2 h, and showed to be tetragonal kesterite of improved crystallinity with the relative density in the 80–93% range. The mechanochemical synthesis from the elements was also applied to make a related kesterite-type telluride $Cu_2ZnSnTe_4$ [21] and stannite Cu_2FeSnS_4 [22].

There are also known examples of studies on the synthesis of kesterite that have used a combined metal sulfide-elemental metal approach. For instance, some relevance to mechanochemistry can be found in the report describing thin film preparation from ethanol slurries of the Cu_2S, Zn, Sn, and S powders that were subsequently milled to make inks for CZST thin film formation [23]. In the more relevant case, nanosized powders of CuS and SnS were mixed with microsized powders of Zn and S and dry ball milled at 550 rpm for up to 4 h [24]. Under selected conditions, nanocrystalline kesterite (av. crystallite size of *ca.* 9–18 nm) of the arguably tetragonal I-42 m space group while of apparent cubic (sphalerite-type) appearance was proposed to form.

In this regard, there has been some controversy regarding structural assignments based solely on powder XRD determinations, especially, when matching the patterns of raw nanopowders from the milling step and related patterns of the annealed products. It seems that the kesterite lattice can tolerate a significant degree of non-stoichiometry, defects, and metal site disorder which all impact the macroscopic structure in a complex way and complicate an unequivocal space group assignment. The assignment may range from the cubic (sphalerite-type) space group for the smallest crystallite sizes around 10 nm to various mostly tetragonal space groups for

better crystallized products with particle sizes in the range of a few tens of nanometer. In our recently published paper on the mechanochemically assisted preparation of kesterite nanocrystalline powders from the constituent elements at the highest available rotation speeds of 900–1000 rpm, proposed is a concept of the cubic pre-kesterite that is formed in the high energy ball milling step under the relatively mild temperature conditions (grinding ball temperature does not exceed some 50–60 °C). Subsequent annealing at 450–550 °C transforms it to the disordered tetragonal kesterite *via* particle recrystallization and metal center reorganization into the kesterite-specific Cu-Zn (disordered) and Cu-Sn metal planes [25]. Interestingly, it appears that the raw pre-kesterite is paramagnetic with no clear UV–vis derived semiconducting properties. The high temperature annealing results in a noticeable decrease of powder magnetism and emergence of the expected and crucial for solar cell applications semiconducting properties of the tetragonal kesterite.

Given the long lasting and widespread presence of copper alloys with zinc (brass) and tin (bronze) in technology, it is rather surprising that they have not yet been tried in combination with sulfur as precursors to kesterite. Such an idea seems to be especially attractive since the alloys could conveniently be prepared *in situ* as reactive nanopowders by a simple high energy ball milling of the metals. Herein, we discuss a new mechanochemically assisted synthesis route to kesterite nanopowders starting with a separate stage of suitable copper alloys formation from the mixed metal powders (2Cu:Zn:Sn), the alloys subsequent reactions with sulfur, and final thermal annealing.

2. Experimental

2.1. Synthesis

2.1.1. Mechanochemical milling

Weighted amounts of commercially available microsized powders of copper Cu (>99%), zinc Zn (>99.9%), and tin Sn (99.85%) (Avantor Performance Materials Poland S.A.) of stoichiometric ratio 2:1:1 totalling *ca.* 7 g were placed in the 20 mL grinding bowl (working surfaces lined up with tungsten carbide WC) of planetary micro mill Pulverisette 7 (Fritsch) together with a set of 80 tungsten carbide WC balls of 5 mm diameter and 7 mL of xylene as a dispersion liquid ("wet" milling conditions). The applied rotation speed was 900 or 1000 rpm. The effective milling time was set at 1–10 h, which was realized by 3-min milling cycles each followed by a 10-min idle period to prevent from bowl overheating. The milling parameters were selected based on preliminary experiments aimed at process optimization towards completion of reactions, in particular, using 80 WC milling balls of 5 mm diameter was suggested by Fritsch as optimum for 20 mL grinding bowl, the high rotation speeds of 900–1000 rpm resulted in approx. cutting the rection times at least by two compared with typically applied speeds of 500–700 rpm, and "wet" milling conditions to minimalize ball abrasion. Upon flashing the bowl's volume with argon Ar, the milling was carried out in the atmoshere of Ar and xylene vapors enclosed in the tightly closed 20 mL bowl. After completion of this step and sampling/removing *ca.* 2 g of the alloyed mixture for characterization, a suitable amount of sulfur S (Avantor Performance Materials Poland S.A., >99.9%) was added to the bowl's content and milling was continued for another 4–10 h. In this regard, the quantity of S, including 2 at.% excess, was calculated based on the target kesterite stoichiometry 2Cu:Zn:Sn:4S taking into account the initial amounts of the metals and the amount of the alloys sample taken for characterization. It is instructive to note that excess of S is advantageous in the process and any remaining quantities of it can easily be removed in the annealing stage due to easy S-evaporation. Finally, the wet mixture was evaporated/dried overnight at room temperature resulting in the black powdery raw product that was quantitatively separated from the milling balls.

2.1.2. Thermal annealing

After sampling the raw product for characterization, it was thermally annealed in an alumina boat crucible at 500 or 550 °C for 6 h under an argon flow of 0.05 L/min. The annealed off-black product was evacuated for 0.5 h at room temperature to afford the target material.

2.2. Characterization

All products were characterized by standard powder XRD analysis (Empyrean PANalytical, Cu K_α source; $2\Theta = 10–110^\circ$). Average crystallite sizes were evaluated from Scherrer's equation applying the Rietveld refinement method. Standard 5-point BET specific surface areas, mesopore surface areas, and average mesopore diameter (the latter two based on BJH theory applied to the desorption part of the isotherm hysteresis) were determined by low temperature nitrogen adsorption on Micromeritics Gemini 2380. Helium densities were obtained by Micromeritics AccuPyc. Solid state MAS NMR spectra were measured on the APOLLO console (Tecmag) at the magnetic field of 7.05T produced by the 300 MHz/89 mm superconducting magnet (Magnex). A Bruker HP-WB high-speed MAS probe equipped with the 4 mm zirconia rotor and KEL-F cap was used to spin the sample. The ^{65}Cu MAS NMR spectra were measured at 85.11 MHz using a single 2 μs rf pulse corresponding to π/4 flipping angle in the liquid. The spinning speed was 6 kHz. The acquisition delay used in accumulation was equal to 10 s and 256 scans were acquired. The frequency scale in ppm was referenced to the ^{65}Cu resonance of CuCl. The ^{119}Sn MAS NMR spectra were measured at 111.68 MHz using a single 3 μs rf pulse corresponding to π/2 flipping angle. The spinning speed was 6 kHz. The acquisition delay used in accumulation was 30 s and 256 scans were acquired. The frequency scale in ppm was secondary-referenced to the central transition of SnS spectrum located at −299 ppm. Micro-Raman analysis was done by HORIBA LabRAM HR spectrometer with 532 nm laser, sample power of 20 mW, accumulation time 10 s and 2 scans, confocal hole 1000 μm with long-focus length. Photoelectron XPS spectra were acquired with Vacuum Systems Workshop Ltd. and Mg anode with photon energy of 1253.6 eV. UV–vis data were collected in the diffuse reflectance mode on a Perkin-Elmer spectrophotometer Lambda 35 equipped with a 50 mm integrating sphere. A disc made of pure $BaSO_4$ was used for background collection whereas a thin layer of product powder

pressed on the disc surface was used for sample acquisition. SEM/EDX data were acquired with a Hitachi Model S-4700 scanning electron microscope.

3. Results and discussion

Based on the observations in our previously investigated mechanochemical system for kesterite synthesis made of four starting elements {2Cu + Zn + Sn+4S} reacting "at once", the limiting factor in the amount of time of raw product formation under the applied conditions was incorporation of Sn into the evolving sphalerite-type cubic phase that had to be subsequently annealed to produce the tetragonal kesterite [25]. Such a cubic phase was seen both in the early stages of the reactions as a growing component in the mixture and, eventually, as the exclusive raw product that was tentatively called by us a pre-kesterite. Interestingly, at any point no additional phases other than unreacted Sn were observed. This stands in contrast to some related reports that have proposed kesterite formation through transient metal sulfides formed upon high energy ball milling of the elements [16,19]. In this regard, we have examined products by powder XRD after manually grinding/mixing the four-element powder mixture in an agate mortar for 10 min. Somewhat surprisingly, in addition to the unreacted microcrystalline starting elements Zn, Sn, and S, the covellite-type nanophase of CuS was the only Cu-bearing component. This result pointed out to very facile reactions of Cu with S yielding the controversial Cu(II) sulfide [26] before any interaction of S with Zn or Sn could have taken place. This can be confronted with the standard enthalpies of formation of the binary sulfides, $\Delta_f H^o$ (kJ/mol) [27]: ZnS, −157; Cu_2S, −46; CuS, −53; SnS, −98; SnS_2, −121, which do not offer any simple explanation for the preferential formation of CuS in the system. It is very likely that tight oxide layers due to particle surface passivation with oxygen of the original Sn and Zn powders could contribute to reaction kinetics by increased activation barriers for their sulfurization giving way to the favored Cu reactions with S and, therefore, setting the course of subsequent reaction steps.

Prior alloying of the metals particles before sulfurization could potentially circumvent such inhomogeneity of the system as well as modify the reaction kinetics towards kesterite by altering metals reactivity towards sulfur. One has to keep in mind that there is a fine interplay between metal solid solutions and intermetallic compounds, all customarily called alloys, which is reflected in their not well understood complex chemistry patterns and specific commercially available materials forms. From a still disputable point of view, the structure of such alloys including intermetallics is best explained by statistical short range order parameters for various atomic clusters, which implies significant disorder in the solid state [28]. In this regard, the phase diagram for the binary system Cu-Sn indicates the occurrence of five stable bimetallic compounds/intermetallics (crystalline phases) [29,30], *i.e.*, $C_{41}Sn_{11}$ (δ), $C_{10}Sn_3$ (ζ), Cu_3Sn (ε), and Cu_6Sn_5 (η'; sometimes labeled as Cu/Sn = 1/1) with the latter having also a high temperature modification η above 180 °C. This is supported by the negative standard enthalpies of formation of the compounds, *e.g.*, $\Delta_f H^o$ (kJ/mol) for Cu_3Sn (ε phase) is −3.91 to −4.10, for Cu_6Sn_5 (η phase) is −2.99, and for Cu_6Sn_5 (η' phase) is −1.99 [31]. It is worth pointing out that the compounds tolerate a certain degree of non-stoichiometry *versus* the formula compositions. For instance, based on the phase diagram, the common monoclinic η phase of Cu_6Sn_5 may have the 43.5–44.3 at.% Sn contents, above which the phase is stable in equilibrium with Sn [32]. When considering the binary system Cu-Zn, there are known five distinct bimetallic compounds [28,31,33,34], *i.e.*, CuZn (β and β'), Cu_5Zn_8 (γ_1 or γ brass, sometimes labeled as Cu/Zn = 5/8), $CuZn_3$ (δ), and $CuZn_4$ (ε). These compounds are also characteristic of negative $\Delta_f H^o$'s (kJ/mol) that are, generally, lower than those in the Cu-Sn system, *e.g.*, for CuZn (β' phase) it is −11.12 and for Cu_5Zn_8 (γ phase) it is −11.41 [31]. Similarly as in the Cu-Sn system, the compounds may show significant non-stoichiometry; in the common phase of the body centered cubic Cu_5Zn_8 (γ brass) the 57–70 at.% Zn contents are possible [32]. In the binary system Sn-Zn, the metals dissolve inconsiderably in each other and they are characterized by a binary phase diagram with an eutectic composition of 91 wt.% Sn and 9 wt.% Zn (or 14.9 at.% of Zn) showing a melting point of 198.5 °C [35]. It is worth mentioning that in the ternary system Cu-Zn-Sn no trimetallic compound was found, therefore, alloying these three metals might result only in the definite binary intermetallics [36]. This is exemplified in the investigations of the sputtered trimetallic Cu-Zn-Sn layers pyrolyzed later in the sulfur or selenium atmosphere where up to 350 °C such crystalline phases as η-$Cu_{6.25}Sn_5$, Cu_5Zn_8, and $Cu_{2-x}S$ were identified [37].

The application of mechanochemistry for making various metallic alloys including their metastable phases have recently been reviewed [38,39]. Among them, selected individual copper bimetallics have been prepared by this route. In the binary system Cu-Sn, milling the compositions with excess Sn for a total time of 400 min at an unspecified rotation speed followed by heat treatment at 150 °C for another 400 min afforded either a pure phase of Cu_6Sn_5 or core-shell composites Cu_6Sn_5/Sn; such products were tried as an anode material for lithium-ion batteries [40]. It is also worth mentioning that the η phase Cu_5Sn_6 appears to be preferentially formed in various systems that involve Cu/Sn-Zn interfaces or films [41,42]. As for the system Cu-Zn, wet ball milling of the metals various mixtures at 200−300 rpm resulted in four binary phases but the zinc-rich phases Cu_5Zn_8 (γ) and $CuZn_4$ (ε) were formed first, presumably, due to much higher diffusivity of copper in zinc than *vice versa* [43]. Attrition milling of the Cu + Zn (1 to 1) mixtures with 2 wt.% of stearic acid was applied at 600−1000 rpm to preferentially produce Cu_5Zn_8 admixed with excess Cu [44]. Some specific Cu/Sn-Zn soldering systems lead to formation of Cu_5Zn_8 as well [45]. There are no known to us reports of milling three metals at once.

Fig. 1 presents the typical XRD patterns obtained for materials from all crucial steps of the synthesis. Specifically, ball milling of the {2Cu + Zn + Sn} stoichiometric mixture of the three-metal powders for 10 h at 900 or 1000 rpm resulted exclusively in two copper intermetallic compounds, *i.e.*, hexagonal Cu_6Sn_5-type η' phase (a = 4.20 Å, c = 5.10 Å, D_{av} = 15 nm; *ca.* 70 wt.% yield) and cubic Cu_5Zn_8-type γ phase (a = 8.90 Å, D_{av} = 12 nm; *ca.* 30 wt.% yield) (Fig. 1A). Similar values for phase amounts and cell parameters were derived for both of the

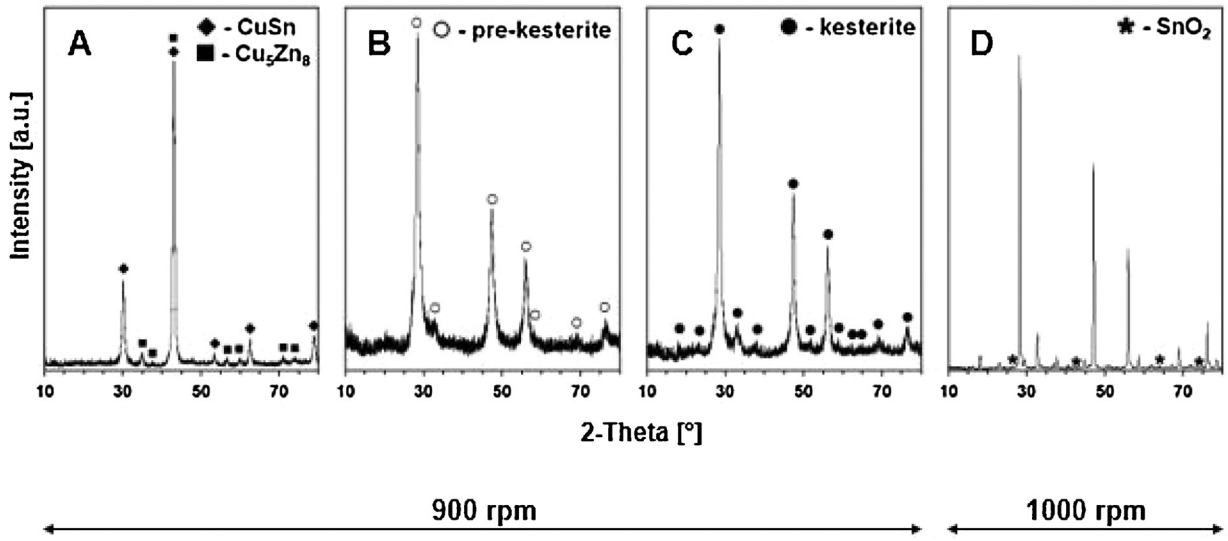

Fig. 1 – Powder XRD patterns for wet ball milled substrate mixtures and products, 900 rpm (A through C) and 1000 rpm (D) [(substrate), milling time]: A – (2 Cu + Zn + Sn, 10 h) to yield alloys; B – (alloys from A + 4S, 10 h) to yield pre-kesterite; C – (pre-kesterite from B, annealed at 500 °C) to yield kesterite; D – (pre-kesterite prepared at 1000 rpm, 4 h alloying, 10 h reaction with S, annealed at 500 °C) to yield kesterite (not marked lines). Note, diffraction patterns for pre-kesterite and kesterite nanopowders are overall similar and differ mainly with a few low intensity peaks present in tetragonal kesterite.

shorter milling times (1 and 4 h). The 10 h milling caused a noticeable decrease of the average particle size of Cu_5Zn_8 from 13 nm (1 h) and 12 nm (4 h) down to 9 nm (10 h). Based on detailed mass balance considerations, it became apparent that the observed proportions of the phases reflected their definite non-stoichiometry *vs.* the respective formulae—the nominal η' phase Cu_6Sn_5 appeared to be Sn-deficient with a formula closer to Cu_6Sn_4 (or, around 40 at.% Sn) while the γ phase Cu_5Zn_8 was Zn-rich approaching the stoichiometry Cu_5Zn_{11} (or, around 69 at.% Zn). The latter composition was within the stability range for the γ phase Cu_5Zn_8 whereas it appeared to be off such a range for the η' phase Cu_6Sn_5 (43.5 at.% < Sn < 44.3 at.%), indicating its metastable characteristics. Given the lack of a stable ternary compound in the system Cu-Zn-Sn, such a compositional outcome of the reactive milling is intuitively justified. First, the identified polytypes of the Cu_6Sn_5-type and Cu_5Zn_8-type are the commonly occurring phases at room temperature for various Cu/Zn/Sn systems [28–37] and, second, the pronounced "non-stoichiometry" of Cu_5Zn_8 might have an origin in the relatively broad composition stability range of the compound [32]. In recapitulating, the detected compounds in our trimetallic system conform well with the ones formed under similar conditions in the related bimetallic systems.

The subsequent 4-h mechanochemical reaction at 900 rpm with sulfur S of the pre-formed *in situ* alloy mixture resulted in the predominant cubic pre-kesterite (a = 5.43 Å; D_{av} = 8 nm) contaminated merely by <1 wt.% of unreacted Cu_6Sn_5 (not shown) whereas the longer reaction time totaling 10 h afforded a pure pre-kesterite (a = 5.42 Å; D_{av} = 8 nm) (Fig. 1B). The annealing of the latter at 500 °C, 6 h, Ar yielded the pure tetragonal kesterite resolved in the space group I-42 m typical for disordered kesterite with random scrambling of Cu and Zn atoms at specific planes (a = 5.44 Å, c = 10.78 Å; D_{av} = 12 nm) (Fig. 1C). A similarly prepared but milled at a higher rotation speed of 1000 rpm kesterite material was shown to be much better crystallized (a = 5.43 Å, c = 10.83 Å; D_{av} = 70 nm) (Fig. 1D, kesterite pattern is not marked) while having a minor impurity of SnO_2 (0.7 wt.%). For several kesterite materials prepared in this study, the tetragonal cell parameters ranged for a = 5.43–5.44 Å and c = 10.78–10.84 Å. It is worth noting that when milling at 900 rpm was applied, the recorded kesterite average crystallite sizes were significantly smaller than those in our earlier investigations of kesterite synthesis *via* ball milling of the four elements at once, *i.e.*, now mostly 12–14 nm *vs.* then 28–60 nm [25]. This adds to an advantageous crystallite size flexibility of the mechanochemical synthesis of kesterite. At the same time, particles in the low nanosized range might show an increased reactivity towards oxidation upon exposure to humid air. In our hands, a several hour long exposure at ambient to humid air of the kesterite shown in Fig. 1C resulted in its substantial oxidation (*ca.* 50 wt.%) to yield such by-products as hydrated copper(II) sulfate, tin(IV) oxide, and zinc(II) sulfate. It is also worth pointing out that a few hour long annealing step at 500–550 °C is potentially prone to scavenging oxidation of sulfide particle surfaces due to remnant oxygen contents in the supposedly neutral purge gases such as nitrogen or argon. We were able to minimize/exclude this effect by avoiding a direct flow of argon over the crucible in this step. Instead, the ceramic reactor with a lid-covered crucible was first flushed with Ar at ambient and the gas flow was re-directed to a bubbler in a side arm while creating an overpressure in the dead-end reactor in another arm during the annealing stage.

The SEM study was consistent with the pronounced nanosized characteristics of the substrates, by-products, and products; however, no definite morphology of crystallites was observed throughout the processing stages. The typical images are reproduced in Fig. 2. They show micrometer-sized

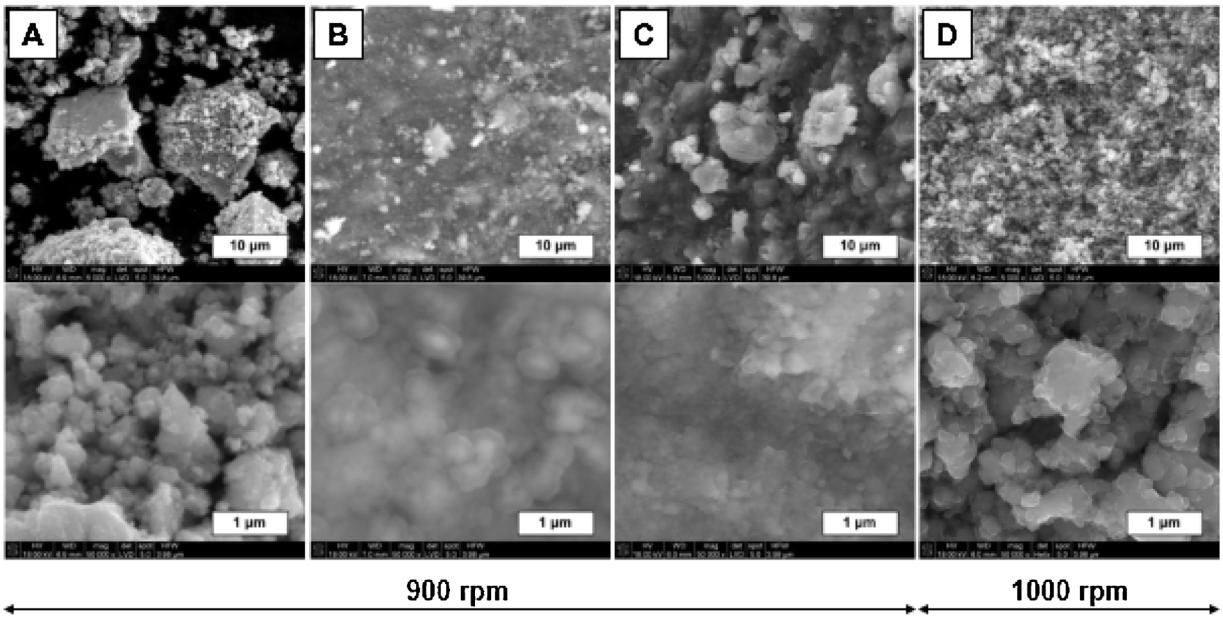

Fig. 2 – SEM images for ball milled substrates and products, 900 rpm (A through C) and 1000 rpm (D) [(substrate), milling time]: A – (2Cu + Zn + Sn, 10 h) to yield alloys; B – (alloys from A + 4S, 10 h) to yield pre-kesterite; C – (pre-kesterite from B, annealed at 500 °C) to yield kesterite; D – (pre-kesterite obtained at 1000 rpm, 4 h alloying, 10 h reaction with S, annealed at 500 °C) to yield kesterite.

agglomerates that tent to be on average smaller and more loose for the alloys mixture (Fig. 2A) than for the pre-kesterite (Fig. 2B) and/or kesterite (Figs. 2C and D). Especially, the bulk appearance of the chunks of pre- kesterite and kesterite points out to their relatively concise microstructure. At higher magnifications, nanosized clustered objects are clearly visible in all samples in accordance with the discussed XRD average crystallite sizes and crystallite agglomeration.

The pore characteristics and the size of specific surface area of both the pre-kesterite and kesterite might become crucial if particle surface derivatization and/or oxidation susceptibility of the products are of interest. Some insight into processing-induced porosity changes of the product nanopowders was acquired from standardized measurements of low temperature nitrogen adsorption. By applying the BET (total porosity) and BJH (mesoporosity) theories, the specific surface areas could be calculated, *i.e.*, the total surface area S_{BET} and mesopore surface area S_{BJH} as well as the relevant average pore diameters as shown for some samples in Table 1. It was found that, generally, the porosity of both the pre-kesterites and kesterites was dominated by mesopores (*D* in the range 2−50 nm), which was confirmed by the similar BET- and BJH-derived surface area values for each of the samples. The annealing of pre-kesterite and formation of kesterite was accompanied by a noticeable decrease of the specific surface area, both S_{BET} and S_{BJH}, as illustrated by the relevant pairs of such materials processed at the various rotation speeds (samples Nos. 2 and 3, 900 rpm: S_{BET} plunged from 28.5 to 1.8 m^2/g; samples Nos. 6 and 7, 1000 rpm: S_{BET} decreased from 40.9 to 21.0 m^2/g). In this regard, the applied higher rotation speed yielded materials with the higher S_{BET}/S_{BJH}'s. Noteworthy were the relatively high surface areas due to mesopores for two related kesterite samples, *i.e.*, No. 7 (500 °C) and No. 8 (550 °C) processed at 1000 rpm, respectively, 21.0 and 27.0 m^2/g.

Also, a surprisingly uniform value of 2.0 Å for the BET average pore diameter D was found for all materials. Another useful information could be derived by comparing the surface areas for two pairs of samples processed at 900 rpm, which differed with milling time after sulfur addition to the pre-formed alloy mixture, *i.e.*, Nos. 1 and 2 and Nos. 4 and 5. It is evident that in both cases increasing that time from 4 to 10 h resulted in the significant 3 to 4-fold increase of the specific surface area whereas the pore size characteristics remained mostly unaffected.

It is presumed that the pre-kesterite—kesterite transformation is mostly associated with metal atom redistribution by diffusion to the thermodynamically favored positions in the tetragonal lattice of the latter. Additionally and significantly, this kind of atom reorganization is accompanied at the annealing temperatures by recrystallization/crystal growth that results in crystallite surface area decrease. As a consequence, the pore structure of the starting pre-kesterite is suitably rebuilt in the kesterite product. It is interesting to refer the discussed porosity data to helium density measurements (d_{He}). Herein, for several samples of pre-kesterite and kesterite d_{He} was determined in the ranges 3.50–3.86 g/cm^3 and 4.02–4.41 g/cm^3, respectively. In our earlier report on the mechanochemical preparation of kesterite from all four elements milled at once these ranges were 3.94–3.99 and 3.94–4.03 g/cm^3 [25]. Specifically, for a series of samples prepared at 1000 rpm (Table 1, samples 7–9) that included the pre-kesterite and the kesterites annealed at 500 and 550 °C, the determined densities were 3.78, 4.21, and 4.41 g/cm^3, respectively. They all could be compared to the theoretical density of 4.56 g/cm^3 for tetragonal kesterite. It is apparent that the

Table 1 – BET- and BJH-derived specific surface area S and average pore diameter D from low temperature nitrogen adsorption for selected pre-kesterite and kesterite samples.

No.	SAMPLE rotation speed: milling times (metals/alloys + S, annealing temp (if any)	BET		BJH	
		S_{BET} [m^2/g]	D_{pore} [nm]	S_{BJH} [m^2/g]	D_{pore} [nm]
1	PRE-KESTERITE 900 rpm: 10 h/4 h	6.8	2.0	6.5	8.2
2	PRE-KESTERITE 900 rpm: 10 h/10 h	28.5	2.0	38.2	11.1
3	KESTERITE 900 rpm: 10 h/10 h 500 °C	1.8	2.0	2.2	14.5
4	PRE-KESTERITE 900 rpm: 1 h/4 h	7.5	2.0	7.9	9.8
5	PRE-KESTERITE 900 rpm: 1 h/10 h	20.6	2.0	30.4	10.1
6	KESTERITE 900 rpm: 1 h/10 h 500 °C	10.7	2.0	10.3	11.6
7	PRE-KESTERITE 1000 rpm: 4 h/10 h	40.9	2.0	53.6	8.1
8	KESTERITE 1000 rpm: 4 h/10 h 500 °C	21.0	2.0	22.3	7.6
9	KESTERITE 1000 rpm: 4 h/10 h 550 °C	27.0	2.0	32.5	6.4

experimental densities of the kesterites constitute 88–97% of the theoretical value and they are usually higher than those of the pre-kesterites. In principle, the mismatch could originate from two major factors. First, in tight agglomerates some helium inaccessible pores (closed pores) could persist and, second, structural defects/non-stoichiometry would impair the sample mass *vs.* sample volume measurements both factors contributing to lower apparent densities. The first aspect might play a role for agglomerates of crystallites in the low nanosized range such as commonly found in pre-kesterite whereas the second one might become significant in kesterite with mostly larger, a few tens nanometer sized crystallites that usually do not form tight agglomerates [46].

Raman spectroscopy has been widely applied to characterize kesterite-type products, mainly, due to its relatively high sensitivity to different crystallographic modifications and detection of low levels of metal sulfide contaminants [47–49]. Fig. 3 shows the typical micro-Raman spectra for the major by-products and products. In the left column, typical spectra for pre-kesterite are presented, all showing at least three superimposed bands at 290–300 cm^{-1} (weak, v. broad), 328–330 cm^{-1} (strong, sharp), and 350–360 cm^{-1} (weak, broad). Additionally, it appears that in the top spectrum (1 h milling, 10 h reaction with S) the typically broad "290–300 cm^{-1}" feature is clearly resolved as a weak 288–290 cm^{-1} peak. In a qualitative approach, all the pre-kesterite spectra are very similar to each other as they are compared to the kesterite spectra shown in the right column. In the latter cases, the peaks seem to be sharper and better separated out, especially, if the 288–290 cm^{-1} peak is concerned.

This could be at least partly due to the larger crystallite sizes of the annealed kesterite compared to the raw milled pre-kesterite. The peaks for kesterite well match the theoretically calculated strongest peaks of A symmetry for this compound [47]. And finally, the spectrum for kesterite annealed at 550 °C has an additional very small intensity peak at 467 cm^{-1} that could be assigned to contamination by Cu_xS [50]; the minute quantity of the compound did not show up in the XRD spectrum, possibly, being below the method's detection limit. The presence of copper sulfide could imply a beginning of nanocrystalline kesterite decomposition upon annealing at temperatures above *ca.* 550 °C.

Significantly, the close resemblance of the cubic pre-kesterite and tetragonal kesterite Raman spectra suggests very similar chemical bonding and lattice phonon characteristics of both related forms supporting our interpretation of their very close structural and chemical features. This similarity was further corroborated by the XPS data (not shown). For the pair of such related materials from the 1000 rpm processing route, *i.e.*, pre-kesterite and 550 °C-annealed kesterite (Table 1, samples 7 and 9, respectively), the spectra for all four elements essentially matched both in terms of peak shape and position/energy as well as the characteristic spread of associated peaks with different spin multiplicity [51]. Thus, in both materials the oxidation states were found to be Cu^{+1}, Zn^{+2}, Sn^{+4}, and S^{-2} (in sulfides) as expected in the formal composition Cu_2ZnSnS_4. Interestingly, there were also very weak sulfur peaks in the position characteristic of S—O bonds such as found in sulfates, which supported some particle surface oxidation in humid air atmosphere during sample handling.

The UV–vis results for all prepared powders were in full accordance with our previously reported findings on the mechanochemically made materials with the pre-kesterite—kesterite characteristics [25].

Namely, all the raw milled powders (pre-kesterite) did not show any definite semiconductive properties whereas the annealed products (kesterite) displayed distinct properties of this kind with a direct band-gap transition in the expected

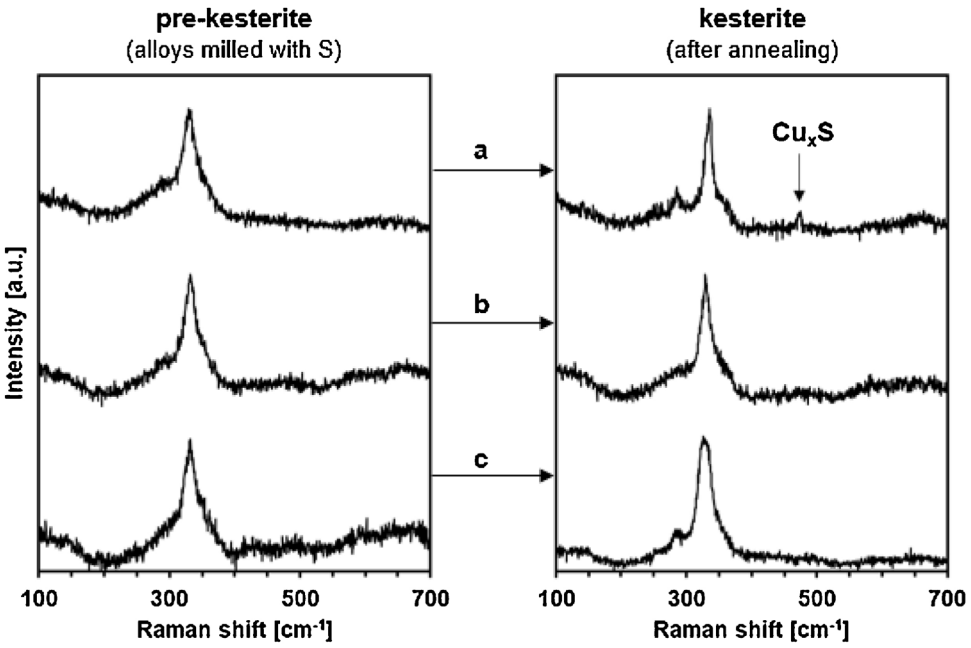

Fig. 3 – Micro-Raman spectra of $\{Cu_6Sn_5+Cu_5Zn_8+S\}$ products milled at 900 rpm. Left column—after milling/alloying metals $\{2Cu+Sn+Zn\}$followed by milling with sulfur S; right column—after annealing at 500 or 550 °C, 6 h, Ar: a) 1 h milling/alloying, 10 h reaction with S, 550 °C, b) 4 h milling/alloying, 10 h reaction with S, 500 °C, c) 10 h milling/alloying, 10 h reaction with S, 500 °C.

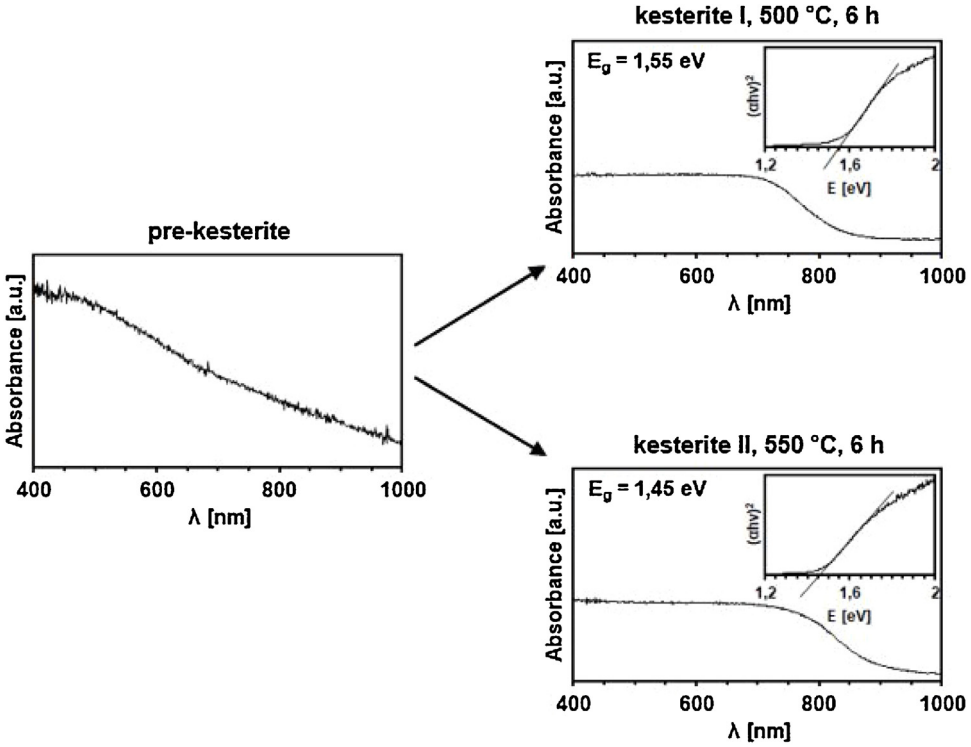

Fig. 4 – UV–vis spectra for selected pre-kesterite (left) and prepared from it kesterite (right) nanopowders, 1000 rpm. Left – pre-kesterite: 4 h metal milling/alloying, 10 h reaction with S. Right – kesterite I (top): 500 °C, 6 h; kesterite II (bottom): 550 °C, 6 h. Kesterite spectra contain inserts of Tauc $(\alpha h\nu)^2$ *vs.* $h\nu$ [energy] plots.

range E_g = 1.4–1.6 eV. This is illustrated in Fig. 4 for one subset of the identically processed materials yet annealed at the different temperatures of 500 and 550 °C with E_g equal to 1.55 and 1.45 eV, respectively, stressing the fundamental difference in their potentials in photovoltaics.

The solid state ^{65}Cu and ^{119}Sn MAS NMR data acquired in this study matched qualitatively the results reported earlier by us for the related kesterite products prepared both from four starting elements {2Cu + Zn + Sn+4S} reacting "at once" [25] and from the selected metal sulfides and sulfur {Cu_2S + ZnS + SnS + S} [52]. First, the pre-kesterite samples from both precursor systems produced no NMR spectra at all. The lack of efficient resonance conditions in this case is proposed to result from d_0 paramagnetism, often detected in various inorganic nanopowders [53] and confirmed by us with EPR measurements [25] and, recently, with extensive magnetic measurements by a SQUID magnetometer [52]. In short, the latter study suggests that the paramagnetism in both the freshly milled pre-kesterite (stronger paramagnetism) and annealed kesterite nanopowders (weaker paramagnetism) can likely be traced to magnetic Cu^{2+}-ions originated from adventitious oxidation of some constituent diamagnetic Cu^{1+}-ions. This property could be at the root of signal broadening beyond detection of resonating ^{65}Cu (quadrupolar with spin 3/2) and ^{119}Sn (spin ½) nuclei in the essentially paramagnetic cubic pre-kesterite lattice. Second, in an example illustrated in Fig. 5, a pair of tetragonal kesterite materials prepared *via* the 1000 rpm processing conditions, namely, those annealed at 500 and 550 °C (samples 8 and 9 in Table 1) clearly showed such spectra with resonances in the expected copper and tin chemical shift ranges. The single ^{65}Cu resonances at 792.8 ppm (500 °C) and 793.3 ppm (550 °C) were both characteristic of quadrupolar-dominated central transition patterns. In ^{119}Sn MAS NMR, a single symmetrical resonance at −127.1 ppm (500 °C) and an asymmetrical resonance with an intense peak at −128.1 ppm (550 °C) were recorded. In our view, that peak asymmetry, which has already been reported in a few relevant studies on kesterite [54,55], may reasonably represent an overlap of distinct neighboring peaks due to different close range environments of definite subsets of tin nuclei. A successful deconvolution of the resonance afforded two peaks at −128.1 and −139.0 ppm with the relative intensities of 0.78 and 0.22, respectively (Table 2).

In this regard, our disordered kesterite with the tetragonal lattice resolved in space group I-42 m is expected to have symmetry differentiated Cu nuclei in the 2a and 2c sites discriminated by distinct S-Cu-S angles as confirmed by the reported ^{65}Cu static NMR experiment resulting in two bands—narrow and wide [54]. The symmetry features can propagate past the S layer to the neighboring Cu-Sn metal layers and inflict close range environment differences onto the Sn nuclei. The reason that we observe two resonances for tin and only one resonance for copper may stem from the fact that in our ^{65}Cu MAS NMR experiments the large quadrupolar coupling could have resulted in the relevant subset of Cu nuclei being undetected. Importantly, if not also for some other reason, this suggests that the ^{65}Cu MAS NMR measurements probe only a certain proportion of the copper nuclei in such a disordered kesterite (*vide infra*).

In our earlier study, the important observation was that the normalized peak intensities in the separate ^{65}Cu or ^{119}Sn MAS NMR spectra for various kesterite samples were significantly different from each other. This indicated that only some of the nuclei, likely, those in suitably ordered close range environments, were actively involved in resonance. Plausibly, the variation in signal intensities could have reflected (i) the proportion of nanoparticle surface atoms *vs.* core atoms and/or (ii) extent of site defects and metal atom substitution inhomogeneity with both factors anticipated to effect in a similar way the local symmetry of electric field gradient and resonance efficiency of both metals nuclei.

In order to estimate a magnitude of this phenomenon, an additional measurement was carried out for kesterite with the higher ^{65}Cu signal intensity from between a pair. A specified amount of Cu(I)Cl (known amount of ^{65}Cu nuclei) was added to a weighted amount of the material annealed at 500 °C and a spectrum was recorded under the same experimental conditions. In Fig. 5, the narrow copper resonance for Cu(I)Cl is located at 0 ppm in the calibration run. This spectrum was first used to calculate a standardized amount of resonant ^{65}Cu nuclei in kesterite with the theoretical formula Cu_2ZnSnS_4 from comparison of both signal intensities assuming that all the ^{65}Cu nuclei resonate in Cu(I)Cl. The calculated amount was then related to signal intensity of the material annealed at 550 °C by applying the same proportionality principle. For both samples, the derived amount of resonant copper nuclei was expressed as a percentage of the total ^{65}Cu nuclei using the theoretical kesterite's formula to calculate the reference number of moles in the samples. These amounts were at 23% and 22% for the 500 and 550 °C annealed kesterites, respectively (Table 2). First, they were comparable, pointing out to similar close range environments of the materials not altered much by the different annealing temperatures. Second and surprisingly, they were rather very low even taking into account a possible slight non-stoichiometry in both samples and a minor contaminant in the 500 °C annealed kesterite (0.7 wt.% SnO_2, see Fig. 1D). One of the reasons for this phenomenon could be the specifics of the MAS resonance experiment in which one of the two copper sites in the disordered kesterite lattice could have gone undetected, as mentioned earlier. However, this is still far from accounting for the majority of the present and potentially resonating nuclei. There must be yet another factor to play a role in such resonance "suppressing". We submit that this could be due to a remnant paramagnetism in the kesterite that now effects merely a definite proportion of nuclei in a similar way as it effects all nuclei in the prevailingly paramagnetic pre-kesterite samples. Since this is thought to be associated with the crucial property of kesterite—light absorption efficiency in the UV–vis range, further related studies are planned. First, they will include synthesis of a wider range of kesterite nanocrystalline powders from different preparation routes mastered in our group and the ^{65}Cu and ^{119}Sn MAS NMR-supported determination of the resonance "supressing" factors, *i.e.*, the percentage of each of the resonating nuclei. Presumably, if the proposed mechanism of remnant paramagnetism is valid, the adjusted suppressing factors should be the same for both nuclei. Second, this will be referred to results of suitable magnetic measurements (EPR, SQUID) that are expected to provide *via* physicochemical correlations

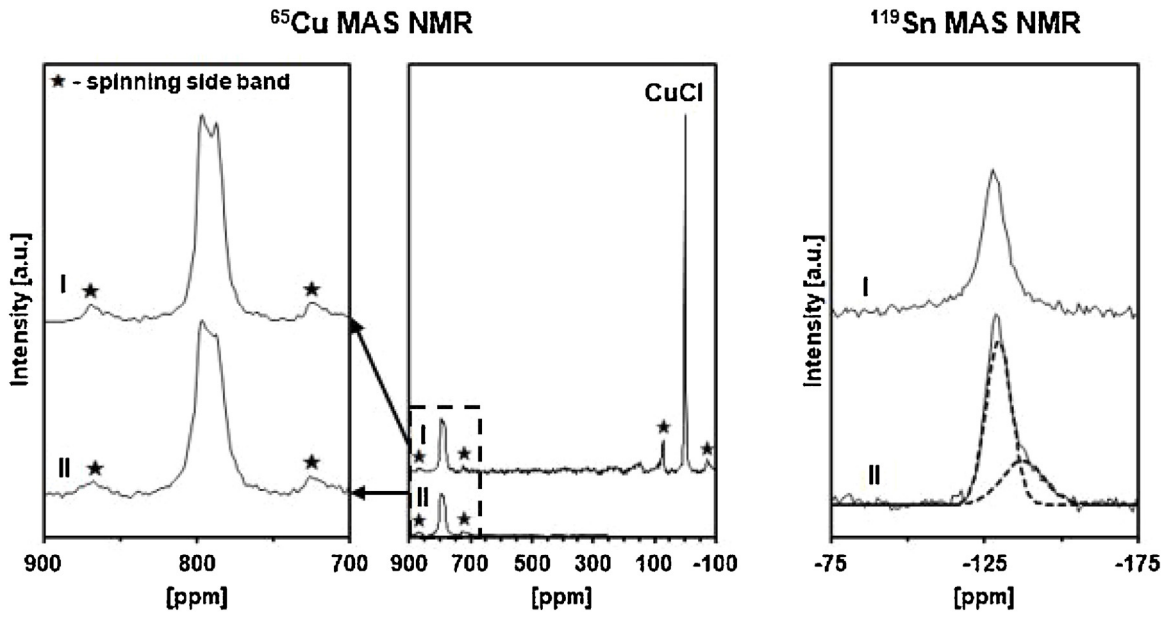

Fig. 5 – Solid state ^{65}Cu and ^{119}Sn MAS NMR spectra for selected kesterite nanocrystalline powders: 4 h metal milling/alloying, 10 h reaction milling with S, 1000 rpm; kesterite I – annealed at 500 °C, 6 h; kesterite II – annealed at 550 °C, 6 h.

Table 2 – ^{65}Cu and ^{119}Sn MAS NMR data for selected kesterite products processed at rotation speed 1000 rpm, milling times 4 h/10 h (metals/alloys + S), and annealed at 500 and 550 °C.

	^{65}Cu MAS NMR		^{119}Sn MAS NMR	
Sample	Annealed at 500 °C	Annealed at 550 °C	Annealed at 500 °C	Annealed at 550 °C
Chemical shift, δ (half-width) [ppm]	792.8 (18.8)	793.3 (21.0)	−127.1 (9.0)	−128.1 (8.6) −139.0 (11.2)
Percentage of resonating nuclei in kesterite [%]	23	22	n/d	n/d

meaningful materials characteristics of kesterite—a broadly variable and hardly predictable semiconductor material.

4. Conclusions

A new mechanochemically assisted synthesis route to the semiconductor kesterite Cu_2ZnSnS_4 nanocrystalline powders *via* the separate high energy ball milling of the constituent metal powders was shown to have distinct advantages over the similar synthesis in which the metal powders were reaction milled with sulfur from the start. In the first all-metal step, a mixture of non-stoichiometric copper alloys/intermetallics of the γ Cu_5Zn_8-type and η' Cu_6Sn_5-type was produced to be further ball milled *in situ* with added sulfur affording a raw product tentatively called a pre-kesterite that showed no semiconducting properties. The thermal annealing of cubic pre-kesterite in the range 500–550 °C resulted in pre-kesterite transformation into the Cu/Zn-site disordered semiconducting tetragonal kesterite. The transient formation of the intermetallics appeared to change favorably the reactivity towards sulfur in the system by minimizing activation barriers, likely, *via* particle surface oxide layer modifications. Upon annealing, the target kesterite nanopowders showed in a few cases remarkably low average crystallite sizes in the range 12–14 nm adding to the method advantages. The application of the high rotation speed of 900 or 1000 rpm was beneficial for shortening of reaction times whereas the different annealing temperatures were found important from the point of view of the magnitude of the UV–vis-derived kesterite band-gap. The ^{65}Cu and ^{119}Sn MAS NMR quantitative estimations of resonance-active atoms pointed out to an utmost importance of kesterite's remnant paramagnetism in defining its semiconducting application potential. In another perspective, the study opens a way to utilization of such waste/commercial copper alloys as bronze and brass for kesterite manufacturing.

Conflicts of interest

The authors declare no conflicts of interest.

REFERENCES

[1] Stroyuk O, Raevskaya A, Gaponik N. Solar light harvesting with multinary metal chalcogenide nanocrystals. Chem Soc Rev 2018;47:5354–422.
[2] Shi Z, Attygalle D, Jayatissa AH. Kesterite-based next generation high performance thin film solar cell: current

progress and future prospects. J Mater Sci Mater Electron 2017;28:2290–306.
[3] Liu XL, Feng Y, Cui HT, Liu FY, Hao XJ, Conibeer G, et al. The current status and future prospects of kesterite solar cells: a brief review. Prog Photovolt Res Appl 2016;24:879–98.
[4] Sun KW, Yan C, Liu FY, Huang JL, Zhou FZ, Stride JA, et al. Over 9% efficient kesterite Cu_2ZnSnS_4 solar cell fabricated by using $Zn_{1-x}Cd_xS$ buffer layer. Adv Energy Mater 2016;6:1600046.
[5] Wang W, Winkler MT, Gunawan O, Gokmen T, Todorov TK, Zhu Y, et al. Device characteristics of CZTSSe thin film solar cells with 12.6% efficiency. Adv Energy Mater 2014;4:1301465.
[6] Shockley W, Queisser HJ. Detailed balance limit of efficiency of p-n junction solar cells. J Appl Phys 1961;32:510–9.
[7] Balaz P, Achimovicova M, Balaz M, Billik P, Cherkezova-Zheleva Z, Criado JM, et al. Hallmarks of mechanochemistry: from nanoparticles to technology. Chem Soc Rev 2013;42:7571–637.
[8] Xu CP, De S, Balu AM, Ojeda M, Luque R. Mechanochemical synthesis of advanced nanomaterials for catalytic applications. Chem Commun (Camb) 2015;51:6698–713.
[9] Balaz P, Balaz M, Achimovicova M, Bujnakova Z, Dutkova E. Chalcogenide mechanochemistry in materials science: insight into synthesis and applications (a review). J Mater Sci 2017;52:11851–90.
[10] Ritscher A, Just J, Dolotko O, Schor S, Lerch M. A mechanochemical route to single phase Cu_2ZnSnS_4 powder. J Alloys Compd 2016;670:289–96.
[11] Ritscher A, Schlosser M, Pfitzner A, Lerch M. Study of the mechanochemical process to crystalline Cu_2ZnSnS_4 powder. Mater Res Bull 2016;84:162–7.
[12] Ritscher A, Franz A, Schorr S, Lerch M. Off-stoichiometric CZTS: neutron scattering investigations on mechanochemically synthesized powders. J Alloys Compd 2016;689:271–7.
[13] He J, Sun L, Zhang KZ, Wang WJ, Jiang JC, Chen Y, et al. Effect of post-sulfurization on the composition, structure and optical properties of Cu_2ZnSnS_4 thin films deposited by sputtering from a single quaternary target. Appl Surf Sci 2013;264:133–8.
[14] Lin YP, Chi YF, Hsieh TE, Chen YC, Huang KP. Preparation of Cu_2ZnSnS_4 (CZTS) sputtering target and its application to the fabrication of CZTS thin-film solar cells. J Alloys Compd 2016;654:498–508.
[15] Wang Y, Gong H. Cu_2ZnSnS_4 synthesized through a green and economic process. J Alloys Compd 2011;509:9627–30.
[16] Gao F, Yamazoe S, Maeda T, Nakanishi K, Wada T. Structural and optical properties of In-free $Cu_2ZnSn(S,Se)_4$ solar cell materials. Jpn J Appl Phys 2012;51:10NC29.
[17] Park BI, Hwang YJ, Lee SY, Lee JS, Park JK, Jeong JH, et al. Solvent-free synthesis of Cu_2ZnSnS_4 nanocrystals: a facile, green, up-scalable route for low cost photovoltaic cells. Nanoscale 2014;6:11703–11.
[18] Shyju TS, Anandhi S, Suriakarthick R, Gopalakrishnan R, Kuppusami P. Mechanosynthesis, deposition and characterization of CZTS and CZTSe materials for solar cell applications. J Sol State Chem 2015;227:165–77.
[19] Pareek D, Balasubramaniam KR, Sharma P. Reaction pathway for synthesis of $Cu_2ZnSn(S/Se)_4$ via mechano-chemical route and annealing studies. J Mater Sci Mater Electron 2017;28:1199–210.
[20] Liu CQ, Wen B, Wang N, Liu SM, Wang HL, Jiang WW, et al. Phase evolution and sintering behaviors of Cu_2ZnSnS_4 powders synthesized by mechanochemical process with different milling parameters. J Alloys Compd 2017;708:428–36.
[21] Pareek D, Balasubramaniam KR, Sharma P. Synthesis and characterization of kesterite $Cu_2ZnSnTe_4$ via ball-milling of elemental powder precursors. RSC Adv 2016;6:68754–9.
[22] Balaz P, Balaz M, Sayagues MJ, Skorvanek I, Zorkovska A, Dutkova E, et al. Mechanochemical solvent-free synthesis of quaternary semiconductor Cu-Fe-Sn-S nanocrystals. Nanoscale Res Lett 2017;12:256.
[23] Woo K, Kim Y, Moon J. A non-toxic, solution-processed, earth abundant absorbing layer for thin-film solar cells. Energy Environ Sci 2012;5:5340–5.
[24] Hegedus M, Balaz P, Balaz M, Siffalovic P, Daneu N, Kanuchova M, et al. Mechanochemical approach to a Cu_2ZnSnS_4 solar cell absorber via a" micro-nano" route. J Mater Sci 2018;53:13617–30.
[25] Kapusta K, Drygas M, Janik JF, Jelen P, Bucko MM, Olejniczak Z. From magnetic cubic pre-kesterite to semiconducting tetragonal kesterite Cu_2ZnSnS_4 nanopowders via the mechanochemically assisted route. J Alloys Compd 2019;770:981–8.
[26] Goh SW, Buckley AN, Lamb RN. Copper(II) sulfide? Miner Eng 2006;19:204–8.
[27] Jackson AJ, Walsh A. Ab initio thermodynamic model of Cu2ZnSnS4. J Mater Chem A Mater Energy Sustain 2014;2:7829–36.
[28] Hong HL, Wang Q, Dong C, Liaw PK. Understanding the Cu-Zn brass alloys using a short-range-order cluster model: significance of specific compositions of industrial alloys. Sci Rep 2014;4:7065.
[29] Massalski TB, Okamoto H. Binary alloy phase diagrams. Materials Park, Ohio: ASM International; 2001.
[30] Fürtauer S, Li D, Cupid D, Flandorfer H. The Cu-Sn phase diagram, part I: new experimental results. Intermetallics 2013;34:142–7.
[31] Yu SP, Wang MC, Hon MH. Formation of intermetallic compounds at eutectic Sn-Zn-Al solder/Cu interface. J Mater Res 2001;16:76–82.
[32] Bochvar N, Lysova E, Rokhlin L, Ivanchenko V. Cu-Sn-Zn (copper-Tin-zinc), materials science International team msit®. In: Effenberg G, Ilyenko S, editors. Non-ferrous metal systems, vol. 11C3. Berlin, Heidelberg: Springer; 2007. p. 422–35. Part 3, Landolt-Börnstein - Group IV Physical Chemistry (Numerical data and functional relationships in science and technology).
[33] Gierlotka W, Chen SW. Thermodynamic descriptions of the Cu-Zn system. J Mater Res 2008;23:258–63.
[34] Tam PD, Tan PD, Hoc NQ, Hai DTP, Binh NT. Order theory of alloy β-CuZn. Proc Natl Conf Theor Phys 2011;36, 195-20.
[35] Moser Z, Dutkiewicz J, Gasior W, Salawa J. The Sn-Zn (tin-zinc) system. Bull Alloy Phase Diagr 1985;6:330–1.
[36] Chou CY, Chen SW. Phase equilibria of the Sn-Zn-Cu ternary system. Acta Mater 2006;54:2393–400.
[37] Jung HR, Shin SW, Suryawanshi MP, Yeo SJ, Yun JH, Moon JH, et al. Phase evolution pathways of kesterite Cu_2ZnSnS_4 and $Cu_2ZnSnSe_4$ thin films during the annealing of sputtered Cu-Sn-Zn metallic precursors. Sol Energy 2017;145:2–12.
[38] Blazquez JS, Ipus JJ, Moreno-Ramirez LM, Alvarez-Gomez JM, Sanchez-Jimenez D, Lozano-Perez S, et al. Ball milling as a way to produce magnetic and magnetocaloric materials: a review. J Mater Sci 2017;52:11834–50.
[39] Dreizin EL, Schoenitz M. Mechanochemically prepared reactive and energetic materials: a review. J Mater Sci 2017;52:11789–809.
[40] Han QG, Yi Z, Cheng Y, Wu YM, Wang LM. Simple preparation of $Cu6Sn_5$/Sn composites as anode materials for lithium-ion batteries. RSC Adv 2016;6:15279–85.
[41] Lee CS, Shieu FS. Growth of intermetallic compounds in the Sn-9Zn/Cu joint. J Korean Inst Electr Electron Mater Eng 2006;35:1661–4.

[42] Oleshkevych A, Zamani A, Kotenko I, Voloshko S, Sidorenko S, Rennie AR. Thermally driven redistribution of phases and components in Cu/Sn thin film. J Alloys Compd 2012;535:108–13.
[43] Pabi SK, Joardar J, Murty BS. Formation of nanocrystalline phases in the Cu-Zn system during mechanical alloying. J Mater Sci 1996;31:3207–11.
[44] Wang KJ, Cai XL, Wang H, Hu J, Zhang YF. Preparation of Cu-Zn alloy by different high energy ball milling. Adv Mater Res 2012;412:259–62.
[45] Chen K-J, Hung F-Y, Lui T-S, Chen L-H, Chen Y-W. Characterizations of Cu/Sn-Zn Solder/Ag interfaces on photovoltaic ribbon for silicon solar cells. IEEE J Photovolt 2015;5:202–5.
[46] Drygas M, Janik JF. Modeling porosity of high surface area nanopowders of the gallium nitride GaN semiconductor. Mater Chem Phys 2012;133:932–40.
[47] Dimitrievska M, Boero F, Litvinchuk AP, Delsante S, Borzone G, Perez-Rodriguez A, et al. Structural polymorphism in ẗkesteriteC̈Cu_2ZnSnS_4: raman spectroscopy and first-principles calculations analysis. Inorg Chem 2017;56:3467–74.
[48] Wang W, Shen HL, Yao HY, Li JZ, Jiao J. Influence of solution temperature on the properties of Cu_2ZnSnS_4 nanoparticles by ultrasound-assisted microwave irradiation. J Mater Sci Mater Electron 2015;26:1449–54.
[49] Fernandes PA, Salomé PMP, da Cunha AF. Study of polycrystalline Cu_2ZnSnS_4 films by Raman scattering. J Alloys Compd 2011;509:7600–6.
[50] Munce CG, Parker GK, Holt SA, Hope GA. A Raman spectroelectrochemical investigation of chemical bath Cu_xS thin films and their modification. Colloids Surf A Physicochem Eng Asp 2007;295:152–8.
[51] Zou C, Zhang LJ, Lin DS, Yang Y, Li Q, Xu XJ, et al. Facile synthesis of Cu_2ZnSnS_4 nanocrystals. CrystEngComm 2011;13:3310–3.
[52] Lejda K, Drygaś M, Janik JF, Szczytko J, Twardowski A, Olejniczak Z. Magnetism of kesterite Cu_2ZnSnS_4 semiconductor nanopowders prepared by mechanochemically assisted synthesis method. Materials 2020;13:3487.
[53] Sundaresan A, Rao CNR. Ferromagnetism as a universal feature of inorganic nanoparticles. Nano Today 2009;4:96–106.
[54] Paris M, Larramona G, Bais P, Bourdais S, Lafond A, Chone C, et al. ^{119}Sn MAS NMR to assess the cationic disorder and the anionic distribution in sulfoselenide $Cu_2ZnSn(S_xSe_{1-x})_4$ compounds prepared from colloidal and ceramic routes. J Phys Chem 2015;C119:26849–57.
[55] Choubrac L, Paris M, Lafond A, Guillot-Deudon C, Rocquefelte X, Jobic S. Multinuclear (^{67}Zn, ^{119}Sn and ^{65}Cu) NMR spectroscopy—an ideal technique to probe the cationic ordering in Cu_2ZnSnS_4 photovoltaic materials. Phys Chem Chem Phys 2013;15:10722–5.